

## Tailor the Functionalities of Metasurfaces Based on a Complete Phase Diagram

Che Qu,<sup>1</sup> Shaojie Ma,<sup>1</sup> Jiaming Hao,<sup>2,†</sup> Meng Qiu,<sup>1</sup> Xin Li,<sup>1</sup> Shiyi Xiao,<sup>1</sup> Ziqi Miao,<sup>1</sup>  
Ning Dai,<sup>2</sup> Qiong He,<sup>1,3</sup> Shulin Sun,<sup>4</sup> and Lei Zhou<sup>1,3,\*</sup>

<sup>1</sup>State Key Laboratory of Surface Physics, Key Laboratory of Micro and Nano Photonic Structures (Ministry of Education) and Physics Department, Fudan University, Shanghai 200433, People's Republic of China

<sup>2</sup>National Laboratory for Infrared Physics, Shanghai Institute of Technical Physics, Chinese Academy of Science, Shanghai 200083, People's Republic of China

<sup>3</sup>Collaborative Innovation Center of Advanced Microstructures, Fudan University, Shanghai 200433, People's Republic of China

<sup>4</sup>Shanghai Engineering Research Center of Ultra-Precision Optical Manufacturing, Green Photonics and Department of Optical Science and Engineering, Fudan University, Shanghai 200433, People's Republic of China

(Received 14 August 2015; published 1 December 2015)

Metasurfaces in a metal-insulator-metal configuration have been widely used in photonics, with applications ranging from perfect absorption to phase modulation, but why and when such structures can realize what functionalities are not yet fully understood. Here, we establish a complete phase diagram in which the optical properties of such systems are fully controlled by two simple parameters (i.e., the intrinsic and radiation losses), which are, in turn, dictated by the geometrical or material properties of the underlying structures. Such a phase diagram can greatly facilitate the design of appropriate metasurfaces with tailored functionalities demonstrated by our experiments and simulations in the terahertz regime. In particular, our experiments show that, through appropriate structural or material tuning, the device can be switched across the phase boundaries yielding dramatic changes in optical responses. Our discoveries lay a solid basis for realizing functional and tunable photonic devices with such structures.

DOI: 10.1103/PhysRevLett.115.235503

PACS numbers: 81.05.Xj, 42.25.-p, 78.20.Bh

Metasurfaces in a metal-insulator-metal (MIM) configuration have attracted much attention recently [1–20]. A *diversified* set of wave-manipulation effects were realized with such systems, including polarization control [2–4], reflection-phase modulation [5–7], perfect absorption [8–11], anomalous light reflection [1,12,13], focusing [14,15], and holograms [16]. It is intriguing that MIM metasurfaces can behave distinctly under slight structural tuning and, thus, realize such diversified applications. However, although simulations can well reproduce the discovered phenomena [2–16], the inherent physics underlying these distinct effects remains obscure. In particular, why and with what parameters can these MIM metasurfaces exhibit certain functionalities are still not fully understood, despite some initial attempts [17–20].

Here we provide a general guidance for designing MIM metasurfaces with tailored functionalities. We employ the coupled-mode theory (CMT) [21–23] to derive a generic phase diagram in which the functionality of a MIM metasurface is governed by two simple parameters, which are, in turn, linked with the system's structural or material details through two relationships that can be derived *analytically* under certain conditions. The derived formulas guide us to experimentally realize a series of terahertz (THz) metasurfaces with distinct (yet well-controlled) functionalities. In particular, functional phase transitions are experimentally demonstrated via tuning the structural or material parameters of the metasurfaces, again assisted by the phase diagram and the analytical relationships. Our

results not only set up a platform to understand the most recent results on MIM metasurfaces [3–16], but more importantly, they also provide a powerful tool to guide the future design and realization of functional or tunable metadevices with unusual properties.

As schematically depicted in Fig. 1(a), a MIM system typically consists of an array of metallic *subwavelength* resonators and a continuous metallic film separated by a thin dielectric spacer. The metallic film prohibits any

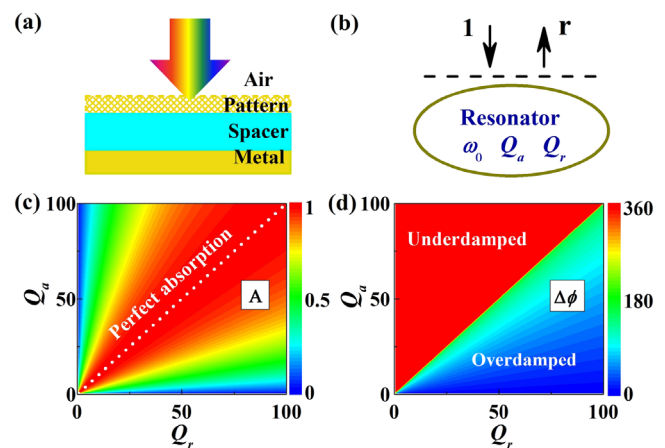


FIG. 1 (color online). Schematics of (a) the MIM system and (b) the single-port resonator model in CMT. Phase diagrams of (c) the on-resonance absorption  $A$  and (d) the span of reflection phase  $\Delta\phi$  versus  $Q_r$  and  $Q_a$  calculated with CMT for the single-port model shown in (b).

transmission through the system so that only the reflection of the device needs to be considered. Near-field coupling between two metallic layers can form a series of resonances at frequencies dictated by the geometrical details, each with induced currents flowing in opposite directions on two metallic layers [24]. When these resonances are well separated in frequency (i.e., the peak width of each mode is much less than the intermode frequency difference), a MIM structure can be well described by a one-port single-mode resonator model as schematically depicted in Fig. 1(b), at frequencies around a particular resonance ( $\omega_0$ ). According to the CMT [21–23], the (complex) reflection coefficient  $r$  of such model is

$$r = -1 + \frac{2/\tau_r}{-i(\omega - \omega_0) + 1/\tau_a + 1/\tau_r}, \quad (1)$$

where  $\tau_a$  and  $\tau_r$  denote the lifetimes of the resonance due to absorption inside the structure and radiation to the far field, respectively. We define two dimensionless parameters  $Q_a = \omega_0\tau_a/2$  and  $Q_r = \omega_0\tau_r/2$  describing, respectively, the absorptive and radiative quality factors of the system.

Equation (1) shows that the physical property of the model is fully determined by  $Q_a$  and  $Q_r$ . A simple calculation reveals that most recently reported behaviors of MIM structures [3–16] can be easily reproduced by tuning these two parameters. Figure 1(c) depicts how the absorbance of our model at its resonance frequency calculated by  $A = 1 - |r|^2$  varies against  $Q_a$  and  $Q_r$ . While perfect absorption  $A = 1$  happens when  $Q_a = Q_r$  (see, also, Refs. [25,26]), the absorbance decreases significantly as it leaves this phase boundary. However, the difference between the two regions separated by this phase boundary *cannot* be clearly seen from the  $|r|^2$  spectra alone. Instead, these two regions can only be distinguished by checking the variation range  $\Delta\phi$  of the reflection phase ( $\phi$ ) in the interested frequency domain. As shown in Fig. 1(d), in the  $Q_a > Q_r$  region where the resonator is underdamped with weak intrinsic absorption,  $\Delta\phi$  can cover the full  $360^\circ$  range with  $\phi$  undergoing a continuous  $-180^\circ$  to  $180^\circ$  variation as frequency passes through the resonance. On the contrary, in the  $Q_a < Q_r$  region where the resonator becomes overdamped, the variation of  $\phi$  only occupies a small range less than  $180^\circ$ . In particular, the involved resonance exhibits a “magnetic” (“electric”) feature in the  $Q_a > Q_r$  ( $Q_a < Q_r$ ) case since we have  $\phi = 0^\circ$  ( $\phi = 180^\circ$ ) at  $\omega = \omega_0$ . Therefore, the competitions between two  $Q$  factors endow the MIM structures a variety of physical properties suitable for different applications. For instance, while a device located in the  $Q_a > Q_r$  region can realize phase-modulation-related effects [2–7,12–16] including polarization control and anomalous reflection, a system with  $Q_a = Q_r$  just behaves as a perfect absorber [8–11], and a resonator located in the  $Q_a < Q_r$  region is a simple electric reflector. More details of the model analyses are presented in Ref. [27].

Having understood the crucial roles of  $Q_a$  and  $Q_r$  in determining the functionality of a MIM metasurface, we derive two analytical formulas to link  $Q_a$  and  $Q_r$  with the structure details of MIM systems with the simplest lateral geometry. Such relationships can help design MIM metasurfaces with tailored functionalities. The schematics of our MIM system is shown in the inset of Fig. 2(a), where the top metallic layer consists of air slits (with widths  $a$ ) arranged with a periodicity  $d$ . The thicknesses of the metallic and dielectric layers are  $h_m$  and  $h$ , respectively. The scattering properties of such a model system under the illumination of a normally incident plane wave with  $\vec{E} \parallel \hat{x}$  can be rigorously studied using the mode-expansion theory (MET) [28,29]. For structures under subwavelength ( $d \ll \lambda$ ,  $h < \lambda$ ) and thin-slit ( $a \ll d$ ) conditions, a simple analytical formula can be derived for the radiation  $Q$  factor [27]:

$$Q_r = \frac{1}{2k_0h} \sum_m \Gamma(m) \frac{\sin^2(m\pi a/d)}{(m\pi a/d)^2}, \quad (2)$$

where  $\Gamma(m) = \epsilon k_0^2 [(2m\pi/d)^2 + \epsilon k_0^2] / [(2m\pi/d)^2 - \epsilon k_0^2]^2$  is a dimensionless parameter to weight the contribution of the  $m$ th mode inside the cavity,  $\epsilon$  is the permittivity of the spacer, and  $\sin^2(m\pi a/d)/(m\pi a/d)^2$  describes the coupling between the external field and the  $m$ th internal mode. Equation (2) is obtained by rigorously calculating  $Q_r$  as

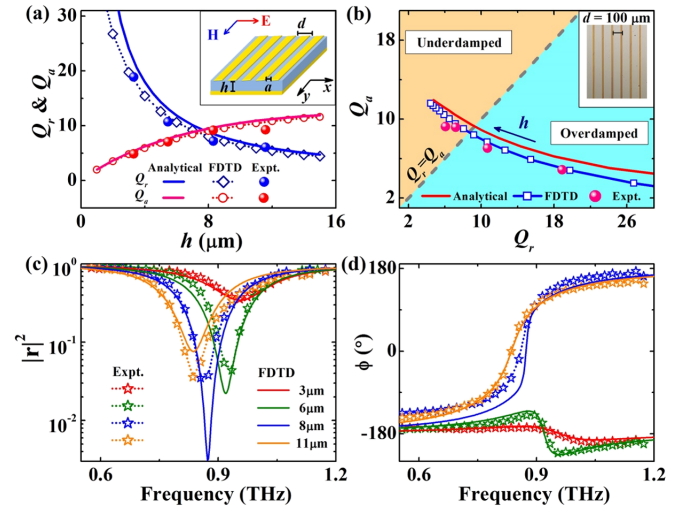


FIG. 2 (color online). (a)  $Q_r$  and  $Q_a$  for a series of metasurfaces (see inset for system geometry) with varying  $h$  obtained by analytical calculations (lines) based on Eqs. (2) and (3) or retrieved from FDTD-simulated spectra (open symbols) and from experimental results (solid symbols). Other geometrical parameters of these metasurfaces are fixed as  $a = 20 \mu\text{m}$ ,  $d = 100 \mu\text{m}$ ,  $h_m = 0.05 \mu\text{m}$ . (b) Replot of the results displayed in (a) in the  $Q_a - Q_r$  phase diagram, where the  $Q_r = Q_a$  line separates the underdamped region (blue) and the overdamped region (orange). Inset shows an optical image of the sample with  $h = 8 \mu\text{m}$ . Spectra of (c) reflectance and (d) reflection phase of four typical samples with  $h$  given in the legend of (c) obtained by THz TDS measurements (symbols) and FDTD simulations (lines).

the ratio of the total energy stored inside the resonator to the energy radiated outside the resonator per time-oscillation cycle based on the field distribution calculated by the MET [27]. Note that we have purposely assumed that both metals and dielectrics are lossless when deriving Eq. (2), since absorptions are explicitly considered when calculating another parameter  $Q_a$ .

We now consider  $Q_a$ , which is defined as the ratio between the total energy  $U$  stored inside the cavity and the energy absorbed by the dielectric spacer  $P_d$  and by the metals  $P_m$ , during a time-oscillation circle. While an analytical expression of  $Q_a$  can also be derived based on the MET [27], here we present a simple and intuitive derivation assuming that the field distributes uniformly inside the cavity. Obviously,  $U$  is proportional to the total volume of the cavity and, thus,  $U \propto \text{Re}(\epsilon) \times hd$ . Meanwhile,  $P_d$  is proportional to  $\text{Im}(\epsilon)\omega_0 \times hd$  since the absorption happens everywhere inside the dielectric medium where  $\text{Im}(\epsilon)$  is nonzero. Finally, considering the exponential decay of the electric field inside a metal layer  $E \sim e^{-z/\delta}$  with  $\delta = \sqrt{2/\mu_0\omega_0\sigma_m}$  being the skin depth, we find that metallic absorption is proportional to the effective field-decaying length  $H(\delta) = \delta(1 - e^{-2h_m/\delta})$ . Collecting all these considerations, we finally have

$$Q_a = \frac{\omega_0 U}{P_d + P_m} = \frac{\text{Re}(\epsilon)hd}{\alpha \text{Im}(\epsilon)hd + \beta(2d - a)H(\delta)}, \quad (3)$$

where  $\alpha$  and  $\beta$  are two parameters to define the relative contributions from the dielectric and metallic media, respectively. Interestingly, Eq. (3) can be derived from the rigorous MET, with expressions of  $\alpha$  and  $\beta$  explicitly given [27].

With Eqs. (2) and (3) at hand, we can effectively “tune” the location of our metasurface in the generic phase diagram [Figs. 1(c) and 1(d)] through varying certain geometrical or material parameters of the metasurface. Consider first the spacer thickness  $h$ . While  $Q_r$  scales inversely with respect to  $h$  [Eq. (2)], which can be attributed to the near-field coupling between two metallic layers,  $Q_a$  almost linearly depends on  $h$  [Eq. (3)]. The distinct  $h$  dependences of two  $Q$  factors are clearly shown in Fig. 2(a), where two lines representing the  $Q_r \sim h$  and  $Q_a \sim h$  relations intersect at a critical point ( $h_c \approx 7.5 \mu\text{m}$ ). Combining Figs. 2(a) and 1, we immediately understand that decreasing  $h$  can drive the system to transit from the underdamped region ( $Q_a > Q_r$ ) to the overdamped one ( $Q_r > Q_a$ ), which is more explicitly illustrated in Fig. 2(b). Noting that the two regions have distinct EM functionalities [see Figs. 1(c) and 1(d)], we, thus, understand that tuning  $h$  can dramatically change the property of a metasurface, especially in the vicinity of  $h \sim h_c$ .

These predictions are verified by our THz experiments and simulations. We fabricated a series of metasurfaces with different  $h$  following standard optical lithography procedures [27]. An optical image of a typical sample is shown in the inset to Fig. 2(b). We next used THz

time-domain spectroscopy (TDS) to measure the spectra of the reflection amplitude or phase of these samples and plot the results in Figs. 2(c) and 2(d)[27]. The measured spectra are in good agreement with finite-difference time-domain (FDTD) simulations on realistic structures, except the case of  $h = 8 \mu\text{m}$ , which is too close to the phase boundary and is, thus, sensitive to perturbations. The distinct behaviors in the phase spectra of different samples [Fig. 2(d)] already imply a phase transition from underdamped to overdamped resonance, as  $h$  decreases from 11 to  $3 \mu\text{m}$ . As a quantitative check, we retrieved the values of two  $Q$  factors by fitting the measured and simulated spectra of different samples to Eq. (1) [27] and depicted the obtained results in Figs. 2(a) and 2(b). Such retrieved values are in reasonable agreement with the model analytical results. In particular, the crossover between two functionality regions is clearly seen in Fig. 2(b).

The slit width  $a$  is another important parameter to modify the properties of a MIM structure. The physics can again be understood using Eqs. (2) and (3). First, we note from Eq. (2) that  $Q_r$  only weakly depends on  $a$ , which is verified by the computed  $Q_r \sim a$  curve depicted in Fig. 3(a), for a model with  $d = 100 \mu\text{m}$  and  $h = 8 \mu\text{m}$  fixed. The physics is that near-field coupling (dictated by  $h$ ) between two metallic layers plays a much more important role than the lateral structural parameter in determining  $Q_r$  of such double-layer systems. Meanwhile, decreasing  $a$  can increase the contribution of metallic absorption through

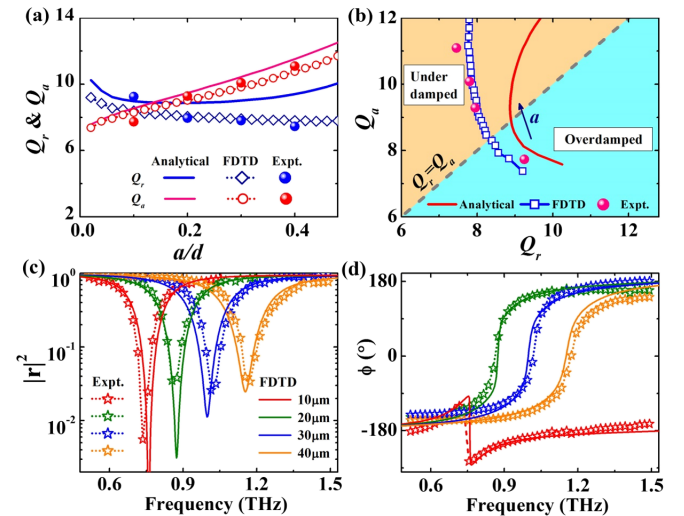


FIG. 3 (color online). (a)  $Q_r$  and  $Q_a$  for a series of metasurfaces with varying slit width  $a$  obtained by analytical calculations (lines) based on Eqs. (2) and (3) or retrieved from FDTD-simulated spectra (open symbols) and experimental results (solid symbols). Other geometrical parameters of these metasurfaces are fixed as  $h = 8 \mu\text{m}$ ,  $d = 100 \mu\text{m}$ ,  $h_m = 0.05 \mu\text{m}$ . (b) Replot of the results displayed in (a) in a  $Q_a - Q_r$  diagram. Spectra of (c) reflectance and (d) reflection phase of four typical samples with  $a$  given in the legend of (c) obtained by THz TDS measurements (symbols) and FDTD simulations (lines).

increasing the metal occupations in the system and, in turn, decrease  $Q_a$  appreciably [see Eq. (3)]. This is verified by the calculated  $Q_a \sim a$  curve for the same model [Fig. 3(a)]. The distinct  $a$  dependences of the two  $Q$  factors creates a crossover point at  $a \approx 14 \mu\text{m}$ . Therefore, a phase transition can be driven by varying the parameter  $a$ , as shown in Fig. 3(b). These predictions are again verified by our THz experiments and FDTD simulations for a series of MIM metasurfaces with a different parameter  $a$  [see Figs. 3(c) and 3(d)]. The retrieved  $Q$  factors from the experiment and FDTD results confirmed the physical picture established above. We note that the discrepancy between analytical and FDTD results becomes large as  $a$  increases [Figs. 3(a) and 3(b)], since Eqs. (2) and (3) are derived based on the narrow-slit approximation ( $a \ll d$ ). However, the overall trend and the phase-region crossover are not affected by such quantitative discrepancies.

Finally, the functionality switching can also be realized by tuning the loss parameters of the constitutional media. It is easily expected that increasing the conductivity  $\sigma_d$  of the dielectric spacer and/or decreasing the conductivity  $\sigma_m$  of the metal can significantly decrease  $Q_a$  through enhancing the absorption, but they have relatively minor effects on  $Q_r$ , which is predominantly determined by the resonator's geometry. Therefore, tuning  $\sigma_d$  and/or  $\sigma_m$  can dramatically affect the device's performances. FDTD simulations were performed to illustrate how the idea works. As shown in Fig. 4(a), increasing  $\sigma_d$  indeed drives the resonator to move downward in the  $Q_r - Q_a$  phase diagram, and a critical transition happens as  $\sigma_d$  equals a particular value. Meanwhile, a similar loss-driven functionality switching is shown in Fig. 4(b) for the case with varying  $\sigma_m$ , where the resonator moves upward in the  $Q_r - Q_a$  phase diagram as  $\sigma_m$  increases. These results point out the possibility of making *tunable* devices based on the MIM metasurfaces. For example, using semiconductors or liquid crystals as the

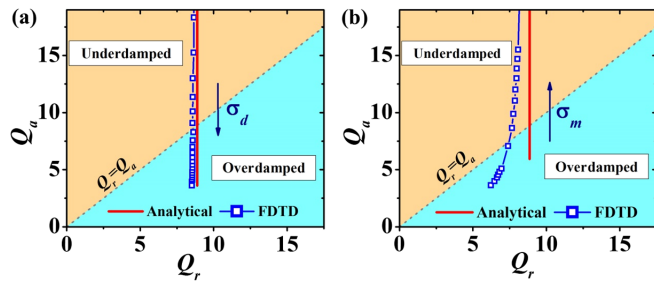


FIG. 4 (color online). (a)  $Q_r$  and  $Q_a$  for a series of metasurfaces with  $\sigma_d$  varying from 8 to 50 S/m and with metal assumed lossless obtained by analytical calculations (circles) based on Eqs. (2) and (3) or retrieved from FDTD-simulated spectra (squares). (b)  $Q_r$  and  $Q_a$  for a series of metasurfaces with  $\sigma_m$  varying from  $5 \times 10^4$  to  $2 \times 10^6$  S/m and with  $\sigma_d$  fixed as 0 S/m obtained by analytical calculations (circles) based on Eqs. (2) and (3) or retrieved from FDTD-simulated spectra (squares). Other parameters are fixed as  $h = 8 \mu\text{m}$ ,  $a = 20 \mu\text{m}$ ,  $d = 100 \mu\text{m}$ ,  $h_m = 0.05 \mu\text{m}$ .

spacer medium, one can tune the loss and/or the dielectric constant of the spacer via optical pumping or electric gating [30–33], which can drive the functionality switching of the MIM device. Alternatively, the conductivity of a graphene can be significantly tuned via electric gate control [34–37], which can also be applied to drive the functionality switching of a MIM system.

Although the above results are for MIM systems with a simple geometry, the conclusions drawn are valid for more complex situations. We now take a metasurface with a cross-shape lateral pattern as an example to explain how the idea works. As shown in Fig. 5(a),  $d$ ,  $l$ , and  $w$  denote the array period, bar length, and bar width, respectively. The role of these parameters can be understood by mapping the present structure to the stripe case studied above. Obviously,  $h$  plays the same role as in previous cases, and the bar length  $l$  is corresponding to  $(d - a)$  in the stripe pattern. However, bar width  $w$  does not have a clear counterpart in the stripe pattern and, thus, has to be studied separately. It is known that a planar resonator with thinner wires exhibits a higher  $Q_r$ , and, thus, decreasing  $w$  must enhance  $Q_r$  of the system. With the roles played by all three parameters known, we can utilize them to guide us in designing appropriate complex MIM structures with desired functionalities. Specifically, to drive a MIM structure from the overdamped region to the underdamped region, one needs to reduce the  $Q_r$  factor through increasing  $h$  and/or  $w$  and enhance the  $Q_a$  factor through increasing  $h$  and/or decreasing  $l$ .

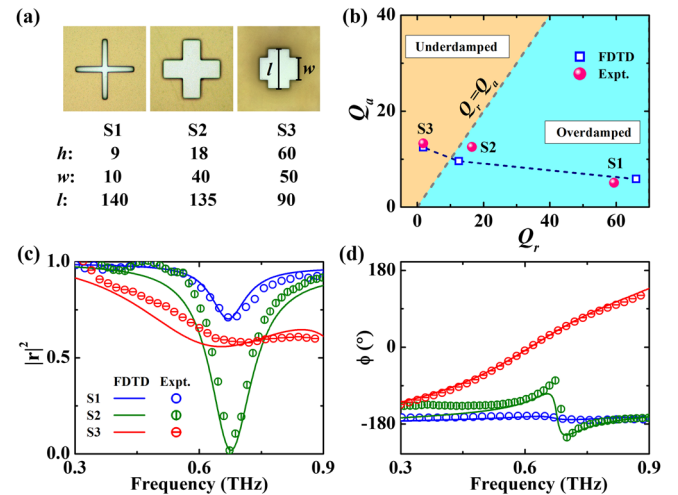


FIG. 5 (color online). (a) Optical images of three fabricated metallic cross-shaped samples (labeled as S1, S2, and S3) with geometrical parameters given in units of  $\mu\text{m}$ . Bright colored areas are occupied by Au. (b)  $Q_r$  and  $Q_a$  for three metasurfaces retrieved from FDTD-simulated spectra (open squares) and retrieved from experimental results (solid symbols). Spectra of (c) reflectance and (d) reflection phase of three samples obtained by THz TDS measurements (symbols) and FDTD simulations (lines).

This prediction is verified by our THz experiments and simulations. Figure 5(a) shows the optical pictures of three typical samples fabricated. Measured spectra of reflection amplitude and phase [Figs. 5(c) and 5(d)] as well as their corresponding retrieved  $Q$  factors [Fig. 5(b)] verify our conjecture. In principle, FDTD simulations demonstrate that smoothly “tuning” the parameters ( $h$ ,  $l$ , and  $w$ ) of a MIM structure can *continuously* change its optical properties and drive the system from one functionality region to another [27]. The experimental samples represent three typical cases, which are a magnetic reflector (sample  $S3$ ), a perfect absorber (sample  $S2$ ), and an electric reflector (sample  $S1$ ). Such generic results are useful for many applications including polarization control [2–4] and holograms [16] which employ anisotropic metasurfaces with similar lateral structures.

In summary, we combine theory and experiments to establish a generic phase diagram to understand the diversified functionalities discovered on MIM metasurfaces and provide practical approaches to tailor the functionalities of such systems. These generic results can guide people to design their own MIM metasurfaces with tailored and even tunable optical responses in different frequency domains. Our analyses also work in the high-frequency domain [27] and for *complex* MIM structures supporting multiple resonances well separated in frequency [27]. However, a naive application of our theory to transmissive metasurfaces [38,39] does not work since a two-port single-mode model does not exhibit similar functionality transitions [27]. These results are discussed in the Supplemental Material [27] in order to stimulate future works.

This work was supported by National Natural Science Foundation of China (Grants No. 11474057, No. 61471345, No. 11174055, No. 11204040, and No. 11404063), the National Young 1000 Talent Plan, MOE of China (Grant No. B06011), and Shanghai Science and Technology Committee (Grants No. 14PJ1409500 and No. 14PJ1401200).

C. Q. and S. M. contributed equally to this work.

\*Corresponding author.

phzhou@fudan.edu.cn

†Corresponding author.

jjaming.hao@mail.sitp.ac.cn

- [1] N. F. Yu and F. Capasso, *Nat. Mater.* **13**, 139 (2014).
- [2] J. M. Hao, Q. J. Ren, Z. H. An, X. Q. Huang, Z. H. Chen, M. Qiu, and L. Zhou, *Phys. Rev. A* **80**, 023807 (2009).
- [3] J. M. Hao, Y. Yuan, L. X. Ran, T. Jiang, J. A. Kong, C. T. Chan, and L. Zhou, *Phys. Rev. Lett.* **99**, 063908 (2007).
- [4] A. Pors, M. G. Nielsen, and S. I. Bozhevolnyi, *Opt. Lett.* **38**, 513 (2013).
- [5] D. Sievenpiper, L. Zhang, R. Broas, N. G. Alexopolous, and E. Yablonovitch, *IEEE Trans. Microwave Theory Tech.* **47**, 2059 (1999).
- [6] L. Zhou, W. Wen, C. T. Chan, and P. Sheng, *Appl. Phys. Lett.* **83**, 3257 (2003).
- [7] A. Pors and S. I. Bozhevolnyi, *Opt. Express* **21**, 27438 (2013).
- [8] H. Tao, C. M. Bingham, A. C. Strikwerda, D. Pilon, D. Shrekenhamer, N. I. Landy, K. Fan, X. Zhang, W. J. Padilla, and R. D. Averitt, *Phys. Rev. B* **78**, 241103 (2008).
- [9] J. M. Hao, J. Wang, X. Liu, W. J. Padilla, L. Zhou, and M. Qiu, *Appl. Phys. Lett.* **96**, 251104 (2010).
- [10] N. Liu, M. Mesch, T. Weiss, M. Hentschel, and H. Giessen, *Nano Lett.* **10**, 2342 (2010).
- [11] C. M. Watts, X. Liu, and W. J. Padilla, *Adv. Mater.* **24**, OP98 (2012).
- [12] S. L. Sun, K.-Y. Yang, C.-M. Wang, T.-K. Juan, W. T. Chen, C. Y. Liao, Q. He, S. Y. Xiao, W.-T. Kung, G.-Y. Guo, L. Zhou, and D. P. Tsai, *Nano Lett.* **12**, 6223 (2012).
- [13] A. Pors, O. Albrektsen, I. P. Radko, and S. I. Bozhevolnyi, *Sci. Rep.* **3**, 2155 (2013).
- [14] X. Li, S. Xiao, B. Cai, Q. He, T. J. Cui, and L. Zhou, *Opt. Lett.* **37**, 4940 (2012).
- [15] A. Pors, M. G. Nielsen, R. L. Eriksen, and S. I. Bozhevolnyi, *Nano Lett.* **13**, 829 (2013).
- [16] W. T. Chen, K.-Y. Yang, C.-M. Wang, Y.-W. Huang, G. Sun, I.-Da Chiang, C. Y. Liao, W.-L. Hsu, H. T. Lin, S. L. Sun, L. Zhou, A. Q. Liu, and D. P. Tsai, *Nano Lett.* **14**, 225 (2014).
- [17] J. Jung, T. Søndergaard, and S. I. Bozhevolnyi, *Phys. Rev. B* **79**, 035401 (2009).
- [18] D. K. Gramotnev, A. Pors, M. Willatzen, and S. I. Bozhevolnyi, *Phys. Rev. B* **85**, 045434 (2012).
- [19] T. Søndergaard, J. Jung, S. I. Bozhevolnyi, and G. D. Valle, *New J. Phys.* **10**, 105008 (2008).
- [20] A. Pors and S. I. Bozhevolnyi, *Opt. Express* **21**, 2942 (2013).
- [21] H. A. Haus, *Waves and Fields in Optoelectronics* (Prentice-Hall, Englewood Cliffs, NJ, 1984).
- [22] S. Fan, W. Suh, and J. D. Joannopoulos, *J. Opt. Soc. Am. A* **20**, 569 (2003).
- [23] W. Suh, Z. Wang, and S. Fan, *IEEE J. Quantum Electron.* **40**, 1511 (2004).
- [24] J. M. Hao, L. Zhou, and C. T. Chan, *Appl. Phys. A* **87**, 281 (2007).
- [25] I. Celanovic, D. Perreault, and J. Kassakian, *Phys. Rev. B* **72**, 075127 (2005).
- [26] D. L. C. Chan, I. Celanovic, J. D. Joannopoulos, and M. Soljačić, *Phys. Rev. A* **74**, 064901 (2006).
- [27] See the Supplemental Material at <http://link.aps.org/supplemental/10.1103/PhysRevLett.115.235503> for more discussions on the phase diagram, derivations of Eqs. (2) and (3), details of simulations, fabrications, and characterizations, the retrieval method to determine  $Q$  factors, additional FDTD results for Fig. 5, high-frequency MIM structures, understanding previous results with our theory, discussions on complex MIM metasurfaces, and the two-port model.
- [28] P. Sheng, R. S. Stepleman, and P. N. Sanda, *Phys. Rev. B* **26**, 2907 (1982).
- [29] F. J. Garcia-Vidal, L. Martín-Moreno, and J. B. Pendry, *J. Opt. A* **7**, S97 (2005).
- [30] H.-T. Chen, W. J. Padilla, J. M. O. Zide, A. C. Gossard, A. J. Taylor, and R. D. Averitt, *Nature (London)* **444**, 597 (2006).
- [31] H.-T. Chen, W. J. Padilla, M. J. Cich, A. K. Azad, R. D. Averitt, and A. J. Taylor, *Nat. Photonics* **3**, 148 (2009).

- [32] G. V. Naik, V. M. Shalaev, and A. Boltasseva, *Adv. Mater.* **25**, 3264 (2013).
- [33] W. Dickson, G. A. Wurtz, P. R. Evans, R. J. Pollard, and A. V. Zayats, *Nano Lett.* **8**, 281 (2008).
- [34] V. Ryzhii, M. Ryzhii, and T. Otsuji, *J. Appl. Phys.* **101**, 083114 (2007).
- [35] B. Sensale-Rodriguez, R. Yan, M. M. Kelly, T. Fang, K. Tahy, W. S. Hwang, D. Jena, L. Liu, and H. G. Xing, *Nat. Commun.* **3**, 780 (2012).
- [36] Yu Yao, M. A. Kats, P. Genevet, N. F. Yu, Y. Song, J. Kong, and F. Capasso, *Nano Lett.* **13**, 1257 (2013).
- [37] Y. Yao, R. Shankar, M. A. Kats, Y. Song, J. Kong, M. Loncar, and F. Capasso, *Nano Lett.* **14**, 6526 (2014).
- [38] N. Yu, P. Genevet, M. A. Kats, F. Aieta, J. P. Tetienne, F. Capasso, and Z. Gaburro, *Science* **334**, 333 (2011).
- [39] N. F. Yu, F. Aieta, P. Genevet, M. A. Kats, Z. Gaburro, and F. Capasso, *Nano Lett.* **12**, 6328 (2012).